THE JOURNAL OF PHYSICAL CHEMISTRY C
A JOURNAL OF THE AMERICAN CHEMICAL SOCIETY

pubs.acs.org/JPCC

Article

Role of the Growth Facet on the Generation and Expansion of Stacking Faults in PVT-Grown *n*-Type 4H-SiC Single-Crystal Boules

Wenhao Geng, Qinqin Shao, Yazhe Wang, Ruzhong Zhu, Xuefeng Han, Xiaodong Pi,* Deren Yang, and Rong Wang*

Cite This: *J. Phys. Chem. C* 2023, 127, 13767−13772

Read Online

ACCESS | Metrics & More | Article Recommendations

ABSTRACT: The generation and expansion of stacking faults (SFs) during the physical-vapor-transport (PVT) growth of *n*-type 4H-SiC single-crystal boules are investigated by combining photochemical etching, transmission electron microscopy, micro-photoluminescence, and micro-Raman investigations. SFs with the Si−C bilayer stacking sequence of (3,3) in Zhdanov's notation are found near the seed crystal of the *n*-type 4H-SiC. Interestingly, we find that the facet region of the *n*-type 4H-SiC single-crystal boule is free of SFs (3,3). Most of the SFs (3,3) are constrained in the nonfaceted region of *n*-type 4H-SiC. Micro-Raman analysis indicates that the shear stress exerted in the nonfacet region gives rise to the formation and expansion of SFs (3,3), which releases the shear stress during the PVT growth of *n*-type 4H-SiC single-crystal boules. Due to the differences of nitrogen concentrations and growth velocities between the facet and nonfacet regions of the *n*-type 4H-SiC single-crystal boule, high compressive stress appears in the interface of the facet and nonfacet regions, which impedes the expansion of SFs (3,3). Furthermore, the shear stress in the facet region of a PVT-grown *n*-type 4H-SiC single-crystal boule is nearly zero, which eliminates the generation and expansion of SFs in the 4H-SiC single-crystal boule.

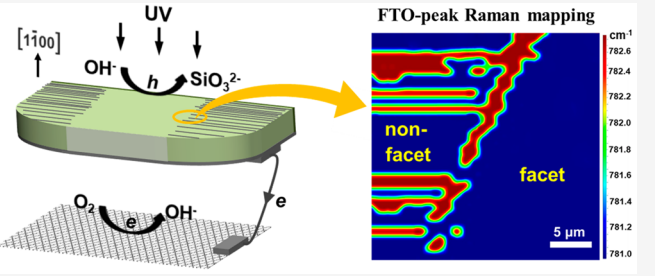

1. INTRODUCTION

4H silicon carbide (4H-SiC) is a promising wide-bandgap semiconductor that has shown great potential in high-power and high-frequency electronics as well as quantum information technologies.[1,2] Physical-vapor-transport (PVT) technology has successfully realized commercialization in the growth of 4H-SiC single-crystal boules.[3,4] During the PVT growth of 4H-SiC single-crystal boules, the generation and expansion of stacking faults (SFs) pose a risk for severe degradation of the quality of 4H-SiC single crystals because the SF energy of 4H-SiC is as low as 14.7 ± 2.5 mJ/m^2.[5] SFs in 4H-SiC serve as the nucleation center of threading dislocations, micropipes, and secondary polymorphs.[6] More importantly, SFs in 4H-SiC substrates may be replicated into homoepitaxial layers, which would degrade the blocking capabilities and reduce the breakdown voltages of 4H-SiC-based high-power devices.[7,8] Therefore, understanding the nucleation and expansion of SFs during the PVT growth of 4H-SiC single-crystal boules is critical to the optimization of 4H-SiC single crystals.

SFs in 4H-SiC can be classified into the Shockley-type SFs and the Frank-type SFs. The Shockley-type SF is created by the in-plane displacement vector, which is separated by two partial dislocations with Burgers vectors of $[10\bar{1}0]\mathbf{a}/3$ and $[01\bar{1}0]\mathbf{a}/3$. Shockley-type SFs can be inherited from the seed crystal or originate from the dissociation of basal plane dislocations.[9,10] The Frank-type SFs are created by climbing of an out-of-plane displacement, which inserts or removes a Si−C bilayer in 4H-SiC. Frank-type SFs are mostly formed by the 2D nucleation or by the conversion from threading screw dislocations (TSDs) during the single-crystal growth.[11,12] Various characterization methods, such as X-ray topography (XRT), photoluminescence (PL), cathodoluminescence (CL), and electroluminescence (EL), have been used to investigate the properties of SFs in 4H-SiC single crystals.[13−17] Transmission electron microscopy (TEM) observations have revealed that the stacking sequences of Si−C bilayers of Shockley-type SFs include (3, 1), (6, 2), (5, 3), and (4, 4) in Zhdanov's notation, and Frank-type SFs have the stacking sequences of (4, 1), (4, 2), and (5, 2). The local PL, CL, and EL investigations indicate that the luminescence peaks of SFs in 4H-SiC locate in the range from 420 to 500 nm.[7,16,18] The transition between a threading edge dislocation (TED) and a Shockley-type SF as well as the transition between a TSD and

Received: March 5, 2023
Revised: June 30, 2023
Published: July 12, 2023

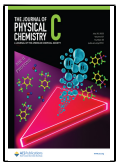

https://doi.org/10.1021/acs.jpcc.3c01502
J. Phys. Chem. C 2023, 127, 13767−13772

a Frank-type SF are also found in XRT, TEM, and EL observations.[13,19] However, these technologies mainly concentrate on the nanoscale atomic structures as well as local electronic and optical properties of a SF in 4H-SiC. Up to now, there has been limited understanding on the formation and expansion mechanisms of SFs during the PVT-growth of 4H-SiC boules.

In this work, we investigate the generation and expansion of SFs during the PVT growth of *n*-type 4H-SiC single-crystal boules by combining photochemical etching, TEM, micro-PL and micro-Raman investigations. SFs with the Si−C bilayer stacking sequence of (3,3) in Zhdanov's notation are found near the seed crystal of *n*-type 4H-SiC. Interestingly, the facet region of the *n*-type 4H-SiC single-crystal boule is free of SFs (3,3). Most of the SFs (3,3) are constrained in the nonfaceted region of *n*-type 4H-SiC. Micro-Raman analysis indicates that the shear stress exerted in the nonfacet region gives rise to the formation and expansion of SFs (3,3), which releases the shear stress during the PVT growth of *n*-type 4H-SiC single-crystal boules. Due to the differences of nitrogen concentrations and growth velocities between the facet and nonfacet regions of the *n*-type 4H-SiC single-crystal boule, the high compressive stress appears in the interface of the facet and nonfacet regions, which impedes the expansion of SFs (3,3). Furthermore, the shear stress in the facet region of a PVT-grown *n*-type 4H-SiC single-crystal boule is nearly zero, which eliminates the generation and expansion of SFs in the *n*-type 4H-SiC single-crystal boule.

2. EXPERIMENTAL SECTION

2.1. Sample Preparation. As shown in Figure 1 (a), nitrogen (N)-doped 4H-SiC single-crystal boules were grown

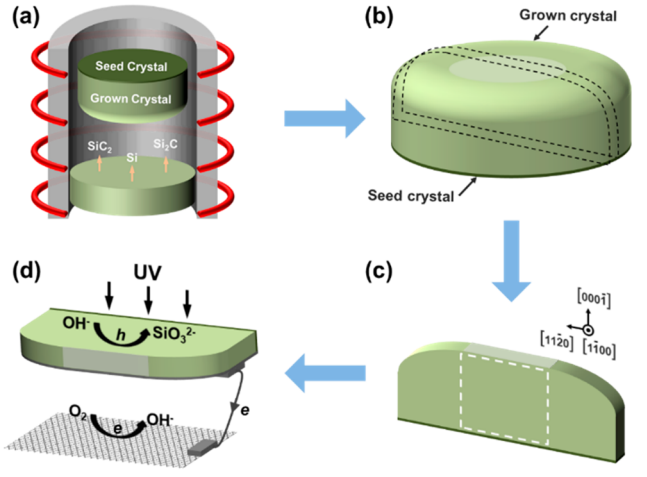

Figure 1. Schematic diagrams of (a) the PVT growth, (b) the vertical slicing of the *n*-type 4H-SiC boule along the growth direction, (c) the obtained *n*-type 4H-SiC (1$\bar{1}$00) wafers with the growth-facet region (within the white dashed frame) and the shoulder region, and (d) the setup of the PCE of *n*-type 4H-SiC (1$\bar{1}$00) wafers.

on the (000$\bar{1}$) plane (C face) of a 4H-SiC seed crystal by the PVT technology, with high-purity N_2 gas being used as the doping source. The growth temperature ranging from 2200 to 2300 °C and the growth pressure ranging from 1 to 10 mbar were adopted. The *n*-type 4H-SiC single-crystal boules were vertically sliced along the growth direction (*c*-axis). After sequential lapping and chemical−mechanical polishing, *n*-type 4H-SiC wafers with nonpolar (1$\bar{1}$00) surfaces were obtained [Figure 1(b)]. As shown in Figure 1(c), the vertically sliced (1$\bar{1}$00) wafer consists of two regions. One region is associated with the growth facet, in which the crystal growth firstly occurs during the PVT growth, and is presented as a convex dome toward the growth direction. The other portion is the shoulder region (nonfacet) near the growth facet, on which the crystal grows slower than that at the growth facet. The *n*-type 4H-SiC (1$\bar{1}$00) wafers were sequentially washed by ultrasonic acetone, ethanol, and deionized water for 15 min and finally immersed in the HF solution to remove surface oxides.

2.2. Photochemical Etching (PCE). Photochemical etching (PCE) was adopted to reveal SFs on the *n*-type 4H-SiC (1$\bar{1}$00) wafer by removing perfect 4H-SiC surrounding SFs. Before PCE, a 100 nm thick titanium (Ti) layer was evaporated on one of the sides of the *n*-type 4H-SiC (1$\bar{1}$00) wafer to enhance the separation of UV-excited electrons and holes. As shown in Figure 1(d), a 500 W Hg lamp was vertically illuminated to the surface of the *n*-type 4H-SiC (1$\bar{1}$00) wafer. Under UV illumination, the selective PCE was carried out in a dilute KOH solution via short-circuiting *n*-type 4H-SiC (1$\bar{1}$00) wafers to a platinum (Pt) net by directly connecting the 4H-SiC sample with the Pt counter electrode. The PCE experiment was carried out in 0.05 M KOH solution for 10 min. The onset potential of the oxygen reduction reaction at Pt is more positive than that of the photoanodic oxidation of *n*-type 4H-SiC, which initiates the photoetching reaction of the *n*-type 4H-SiC sample.[20] During the PCE of the perfect region of *n*-type 4H-SiC, the UV-generated electron−hole pairs are separated by the electric field of the surficial space-charge layer. The UV-generated electrons (e) transporting to the Pt net via the circuit are captured by the dissolved oxygen and form OH^- species by $O_2 + 2H_2O + 4e \rightarrow 4OH^-$. The holes ($h$) are left at the face of the *n*-type 4H-SiC (1$\bar{1}$00) wafer and participate in the oxidation and dissolution of the perfect region of *n*-type 4H-SiC by $SiC + 10OH^- + 8h \rightarrow SiO_3^{2-} + CO_2\uparrow + 5H_2O$.[21] Because SFs in 4H-SiC crystals have been identified as quantum wells for highly efficient recombination of UV-generated electrons and holes,[20,22] UV-generated holes are only involved in the oxidation and removal of the *n*-type 4H-SiC perfect region during the PCE, and SFs appear on the *n*-type 4H-SiC (1$\bar{1}$00) wafer surface in some sort of convex forms.

2.3. Characterization. The surface morphologies of *n*-type 4H-SiC samples after PCE were examined by differential interference contrast (DIC) optical microscopy (Novel, NMM-820TRF) and atomic force microscopy (AFM) (Bruker, Dimension XR). Micro-Raman spectroscopy and photoluminescence spectroscopy were obtained by using a HORIBA LabRAM Odyssey and were excited by lasers of 532 and 266 nm, respectively. TEM specimens were fabricated by using a scanning electron microscope (SEM) (Thermo Scientific, Helios 5 UX) focused ion beam (FIB) microscope with an energy of 1 nA Ga^+ for final milling. TEM observations were performed in a transmission electron microscope (Thermo Scientific, Talos F200X) operated at 200 kV, and a Themis Z (Thermo Scientific, America) microscope equipped with a probe-side Cs corrector operating at 200 kV.

3. RESULTS AND DISCUSSION

Figure 2(a) shows the OM image of an *n*-type 4H-SiC sample after 10 min of PCE. It is clear that high density of horizontal lines appears along the [1$\bar{1}$20] direction on the *n*-type 4H-SiC

https://doi.org/10.1021/acs.jpcc.3c01502
J. Phys. Chem. C 2023, 127, 13767−13772

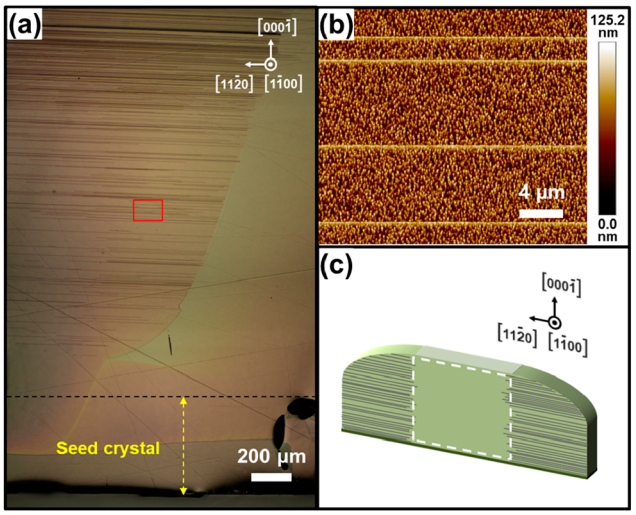

Figure 2. (a) OM image and (b) AFM image of the photochemically etched *n*-type 4H-SiC (1$\bar{1}$00) wafer. (c) is the schematic diagram showing the distribution of horizontal lines in the photochemically etched *n*-type 4H-SiC (1$\bar{1}$00) wafer.

(1$\bar{1}$00) wafer near the seed crystal. These horizontal lines exhibit as horizontal ridges with a height of 125 nm on the (1$\bar{1}$00) surface of *n*-type 4H-SiC [Figure 2(b)]. Interestingly, we find that these horizontal ridges tend to terminate around the growth-facet region, forming a distinct boundary along the crystal growth direction [Figure 2(c)].

Cross-sectional TEM analysis is then carried out to identify the atomic structure of the horizontal-ridge defects on the photochemically etched *n*-type 4H-SiC(1$\bar{1}$00) wafer. The FIB sampling region is taken at the end of the horizontal-ridge defect, as shown by the red frame in Figure 3(a). TEM observations are carried out along the [11$\bar{2}$0] direction, which is indicated by the red arrow in Figure 3(a). Dark-field TEM (DF-TEM) images of the sample acquired under two beam conditions with diffraction vectors ($\boldsymbol{g}$) of [1$\bar{1}$00] and [0004] are shown in Figure 3(b,c), respectively. It is found that the horizontal-ridge defect has a bright contrast with the diffraction vector of [1$\bar{1}$00]. The contrast of the defect disappears with the diffraction vector of [0004]. According to the $\boldsymbol{g}\cdot\boldsymbol{b}$ contrast analysis, this type of the horizontal-ridge defect is attributed to Shockley-type SF.[9,13,23] High-angle annular dark-field scanning TEM (HAADF-STEM) further verifies that the atomic structure of the horizontal-ridge defect is a SF, with the stacking sequence of (3,3) in Zhdanov's notation. The stacking sequence of the Si−C bilayers of the horizontal-ridge region is identical to that of 6H-SiC.[24,25]

The micro-PL spectra are adopted to investigate the stacking sequences of the overall SFs revealed by the PCE of *n*-type 4H-SiC. As shown in Figure 3(e), the band-edge emission at 390 nm and the broad-band emission ranging from 450 to 650 nm are found in the perfect *n*-type 4H-SiC [(1$\bar{1}$00)] sample and the SF region. Similar to previous research, the broad-band emission is attributed to oxygen complexes in 4H-SiC.[26−29] In addition, the emission band centered at 426 nm appears on the PL spectra of the SF region, which is the same as the band-edge emission of 6H-SiC.[30,31] The intensity mapping of the PL peak located at 426 nm is carried out across several horizontal-ridge SFs. As shown in Figure 3(f), all SFs have a higher PL intensity at 426 nm, indicating that the SFs revealed by the PCE in this work have the Si−C stacking sequence of (3,3). Combined with the distribution of horizontal-ridge defects across the *n*-type 4H-SiC (1$\bar{1}$00) sample, we find that the SFs (3,3) may concentrate on the region below the nonfacet region but barely expand to the facet region of the *n*-type 4H-SiC boule.

Micro-Raman spectroscopy is then used to verify the distribution of SFs (3,3) across the *n*-type 4H-SiC (1$\bar{1}$00)

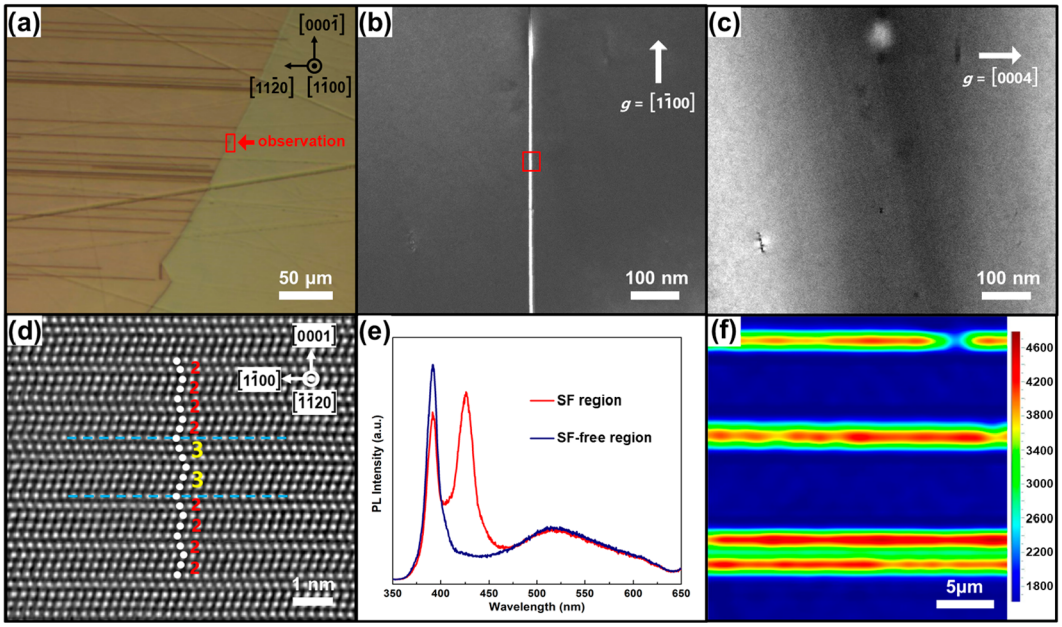

Figure 3. (a) OM image, schematic FIB sampling point (red box), and observation direction of the photochemically etched *n*-type 4H-SiC (1$\bar{1}$00) wafer. The cross-sectional DF-TEM images with electron beam diffraction vectors (b) g = [1$\bar{1}$00] and (c) g = [0004]. The cross-sectional HAADF-STEM image at the red box location is in Figure 3(b). (e) Micro-PL spectra and collected on and off SFs and (f) micro-PL mapping based on the intensity of peaks located at 426 nm of the photochemically etched *n*-type 4H-SiC (1$\bar{1}$00) wafer.

https://doi.org/10.1021/acs.jpcc.3c01502
J. Phys. Chem. C 2023, 127, 13767−13772

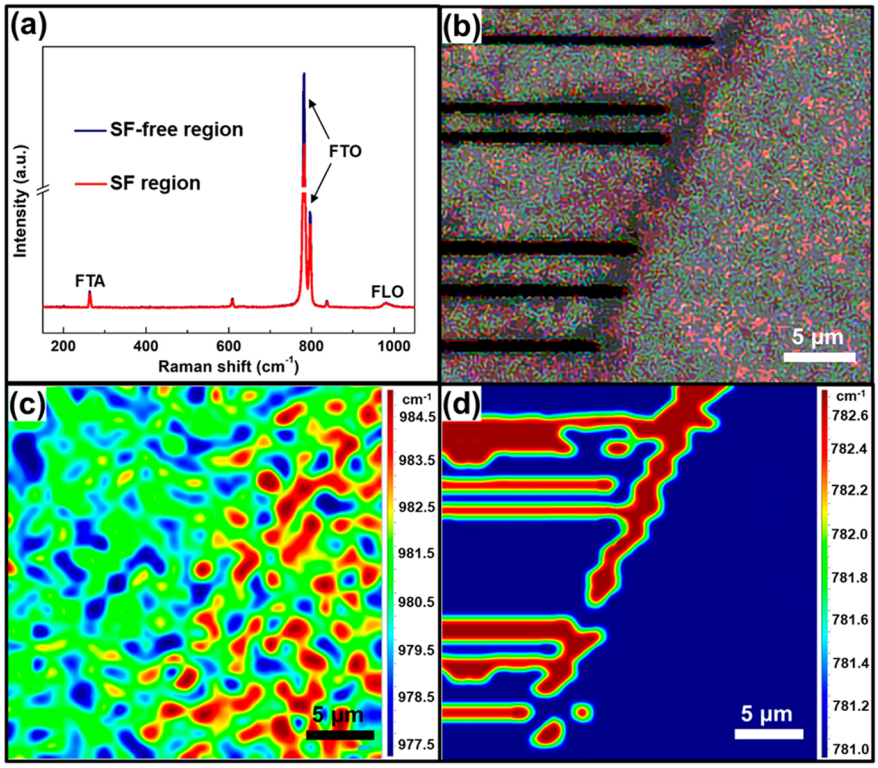

Figure 4. (a) Micro-Raman spectra, (b) OM image, (c) FLO-peak mapping, and (d) FTO-peak mapping of the photochemical etched *n*-type 4H-SiC $(1\bar{1}00)$ wafer.

sample. As shown in Figure 4(a), the transverse acoustic branch (FTA) located at 266 cm^{-1}, the folded modes of the transverse optical branches (FTO) located at 781 and 796 cm^{-1}, as well as the folded mode of the longitudinal optical branches (FLO) located at 980 cm^{-1}[32,33] are observed in both the SFs and the SF-free region of the *n*-type 4H-SiC $(1\bar{1}00)$ wafer. The intensities of the FTA mode and FTO mode of the SF region are lower than those of the SF-free region, indicating structural distortions in the SF region. Because the growth-facet region has a higher N concentration[34,35] and thus a higher free-electron concentration, the peak position of FLO in the facet region should shift to higher wavenumbers.[33] Therefore, the FLO-peak mapping is used to investigate the distribution of SFs along the growth facet of the vertically sliced *n*-type 4H-SiC sample. Figure 4(b) shows the OM image of SFs near the growth-facet region, and Figure 4(c) displays the FLO-peak mapping of the same region. Clearly, the FLO peak of the SF-containing region has low wavenumbers, while the FLO peak of the SF-free region has higher wavenumbers. This verifies that the SFs (3,3) are generated in the nonfacet region, and the growth facet forbids the expansion of the SFs (3,3) during the PVT-growth of the *n*-type 4H-SiC boule. It has been found that the formation and glide motion of basal plane dislocations (BPDs) during the homoepitaxy of 4H-SiC is reduced in the facet trace region.[36] Our work indicates that the reduced formation of BPDs in the facet trace region may be caused by the nearly zero distribution of SFs (3,3) in the facet region of *n*-type 4H-SiC substrates.

It is reported that during the PVT growth of 4H-SiC single crystals, a large amount of thermoelastic shear stress caused by a temperature gradient in the crystal is introduced in the nonfacet region, while the facet region is almost none,[37−39] which may forbid the expansion of SFs (3,3) generated in the nonfacet region. In order to verify the stress distribution across the facet and nonfacet regions, we plot the FTO-peak mapping of the region in Figure 4(b). As shown in Figure 4(d), the interface between the facet and nonfacet regions of *n*-type 4H-SiC has prominent higher wavenumbers because of the differences of N concentration and growth velocity between the facet and nonfacet region.[35] In addition, the FTO-peak positions of SFs (3,3) tending to abruptly shift toward higher wavenumbers always occurs, implying that the compressive strain exists in SFs (3,3).[38,40] This indicates that the shear stress exerted in the nonfacet region is released by the formation and expansion of SFs (3,3), due to the low formation energies of SFs in *n*-type 4H-SiC. Once the expansion of SFs (3,3) reaches the interface of the facet and nonfacet regions, the compressive stress impedes the expansion of SFs (3,3). Furthermore, the shear stress in the facet region of a PVT-grown *n*-type 4H-SiC single-crystal boule is nearly zero, which eliminates the generation and expansion of SFs in the *n*-type 4H-SiC single-crystal boule.

At last, we discuss the effect of doping on the distribution of SFs in PVT-grown high-purity semi-insulating (HPSI) and *p*-type 4H-SiC single-crystal boules. In *n*-type 4H-SiC single-crystal boules, the formation of SFs (3,3) originates from the thermal shear stress in the nonfacet region, and the expansion of SFs (3,3) is impeded by the compressive stress due to different N-doping concentrations in the facet and nonfacet regions of 4H-SiC single crystals. In PVT-grown HPSI 4H-SiC single-crystal boules, SFs (3,3) could be formed due to the thermal shear stress in the nonfacet region, but the expansion of SFs (3,3) might not be impeded in the nonfacet region, because the concentrations of unintentional induced impurities throughout the single crystal are on the same order of magnitude. In PVT-grown *p*-type 4H-SiC single-crystal boules,

https://doi.org/10.1021/acs.jpcc.3c01502
J. Phys. Chem. C 2023, 127, 13767−13772

the formation of SFs (3,3) could also happen in the nonfacet region, and the expansion of SFs (3,3) depends on the doping concentrations of aluminum in the facet and nonfacet regions.

4. CONCLUSIONS

In summary, we have systematically explored the generation and expansion mechanism of SFs in PVT-grown *n*-type 4H-SiC single-crystal boules. By combining PCE, TEM, micro-PL, and micro-Raman investigations, we find that high density of SFs (3,3) appears near the seed crystal of 4H-SiC. More importantly, the generation and expansion of SFs (3,3) are mainly constrained in the nonfacet region of the *n*-type 4H-SiC boule. During the PVT growth of *n*-type 4H-SiC single-crystal boules, the shear stress exerted in the nonfacet region gives rise to the formation and expansion of SFs (3,3), which releases the shear stress. Once the expansion of SFs (3,3) reaches the interface of the facet and nonfacet regions, the compressive stress impedes the expansion of SFs (3,3). Furthermore, the shear stress in the facet region of a PVT-grown *n*-type 4H-SiC single-crystal boule is nearly zero, which eliminates the generation and expansion of SFs in the *n*-type 4H-SiC single-crystal boule.

AUTHOR INFORMATION

Corresponding Authors

Rong Wang − *State Key Laboratory of Silicon and Advanced Semiconductor Materials & School of Materials Science and Engineering, Zhejiang University, Hangzhou 310027, China; Institute of Advanced Semiconductors & Zhejiang Provincial Key Laboratory of Power Semiconductor Materials and Devices, ZJU-Hangzhou Global Scientific and Technological Innovation Center, Zhejiang University, Hangzhou 311200, China;* orcid.org/0000-0003-3333-0180; Email: rong_wang@zju.edu.cn

Xiaodong Pi − *State Key Laboratory of Silicon and Advanced Semiconductor Materials & School of Materials Science and Engineering, Zhejiang University, Hangzhou 310027, China; Institute of Advanced Semiconductors & Zhejiang Provincial Key Laboratory of Power Semiconductor Materials and Devices, ZJU-Hangzhou Global Scientific and Technological Innovation Center, Zhejiang University, Hangzhou 311200, China;* orcid.org/0000-0002-4233-6181; Email: xdpi@zju.edu.cn

Authors

Wenhao Geng − *State Key Laboratory of Silicon and Advanced Semiconductor Materials & School of Materials Science and Engineering, Zhejiang University, Hangzhou 310027, China; Institute of Advanced Semiconductors & Zhejiang Provincial Key Laboratory of Power Semiconductor Materials and Devices, ZJU-Hangzhou Global Scientific and Technological Innovation Center, Zhejiang University, Hangzhou 311200, China*

Qinqin Shao − *State Key Laboratory of Silicon and Advanced Semiconductor Materials & School of Materials Science and Engineering, Zhejiang University, Hangzhou 310027, China; Institute of Advanced Semiconductors & Zhejiang Provincial Key Laboratory of Power Semiconductor Materials and Devices, ZJU-Hangzhou Global Scientific and Technological Innovation Center, Zhejiang University, Hangzhou 311200, China*

Yazhe Wang − *Institute of Advanced Semiconductors & Zhejiang Provincial Key Laboratory of Power Semiconductor Materials and Devices, ZJU-Hangzhou Global Scientific and Technological Innovation Center, Zhejiang University, Hangzhou 311200, China*

Ruzhong Zhu − *Institute of Advanced Semiconductors & Zhejiang Provincial Key Laboratory of Power Semiconductor Materials and Devices, ZJU-Hangzhou Global Scientific and Technological Innovation Center, Zhejiang University, Hangzhou 311200, China*

Xuefeng Han − *Institute of Advanced Semiconductors & Zhejiang Provincial Key Laboratory of Power Semiconductor Materials and Devices, ZJU-Hangzhou Global Scientific and Technological Innovation Center, Zhejiang University, Hangzhou 311200, China*

Deren Yang − *State Key Laboratory of Silicon and Advanced Semiconductor Materials & School of Materials Science and Engineering, Zhejiang University, Hangzhou 310027, China; Institute of Advanced Semiconductors & Zhejiang Provincial Key Laboratory of Power Semiconductor Materials and Devices, ZJU-Hangzhou Global Scientific and Technological Innovation Center, Zhejiang University, Hangzhou 311200, China*

Complete contact information is available at: https://pubs.acs.org/10.1021/acs.jpcc.3c01502

Author Contributions

W.G. and Q.S. contributed equally.

Notes

The authors declare no competing financial interest.

ACKNOWLEDGMENTS

This work is supported by National Natural Science Foundation of China (Grant No. 62274143), "Pioneer" and "Leading Goose" R&D Program of Zhejiang (Grant No. 2022C01021, 2023C01010), Fundamental Research Funds for the Central Universities (Grant No. 226-2022-00200), and Natural Science Foundation of China for Innovative Research Groups (Grant No. 61721005).

REFERENCES

(1) Li, J.; Yang, G.; Liu, X.; Luo, H.; Xu, L.; Zhang, Y.; Cui, C.; Pi, X.; Yang, D.; Wang, R. Dislocations in 4H silicon carbide. *J. Phys. D: Appl. Phys.* **2022**, *55*, 463001.

(2) Yang, G.; Luo, H.; Li, J.; Shao, Q.; Wang, Y.; Zhu, R.; Zhang, X.; Song, L.; Zhang, Y.; Xu, L.; et al. Discrimination of dislocations in 4H-SiC by inclination angles of molten-alkali etched pits. *J. Semicond.* **2022**, *43*, 122801.

(3) Zhong, G.; Xie, X.; Wang, D.; Wang, X.; Sun, L.; Yang, X.; Peng, Y.; Chen, X.; Hu, X.; Xu, X. Growth of *p*-type 4H-SiC single crystals by physical vapor transport using *p*-type SiC powder. *CrystEngComm* **2022**, *24*, 7861−7868.

(4) Mitani, T.; Eto, K.; Komatsu, N.; Hayashi, Y.; Suo, H.; Kato, T. Reduction of threading screw dislocations in 4H-SiC crystals by a hybrid method with solution growth and physical vapor transport growth. *J. Cryst. Growth* **2021**, *568*−*569*, 126189.

(5) Hong, M. H.; Samant, A. V.; Pirouz, P. Stacking fault energy of 6H-SiC and 4H-SiC single crystals. *Philos. Mag. A* **2000**, *80*, 919−935.

(6) Shao, Q.; Geng, W.; Xu, S.; Chen, P.; Zhang, X.; Shen, R.; Tian, H.; Pi, X.; Yang, D.; Wang, R. Nucleation of Treading Dislocations in 4H-SiC at Early Physical-vapor-transport Growth Stage. *Cryst. Growth Des.* **2023**, *23*, 5204.

(7) Yao, Y.; Ishikawa, Y.; Sugawara, Y.; Sato, K.; Shirai, T.; Danno, K.; Suzuki, H.; Sakamoto, H.; Bessho, T.; Dierre, B.; et al. Cross-sectional observation of stacking faults in 4H-SiC by KOH etching on

nonpolar {1−100} face, cathodoluminescence imaging, and transmission electron microscopy. *Jpn. J. Appl. Phys.* **2014**, *53*, 081301.
(8) Chen, B.; Matsuhata, H.; Kumagai, K.; Sekiguchi, T.; Ichinoseki, K.; Okumura, H. Direct imaging and optical activities of stacking faults in 4H-SiC homoepitaxial films. *J. Appl. Phys.* **2012**, *111*, 053513.
(9) Nishio, J.; Okada, A.; Ota, C.; Iijima, R. Direct confirmation of structural differences in single Shockley stacking faults expanding from different origins in 4H-SiC PiN diodes. *J. Appl. Phys.* **2020**, *128*, 085705.
(10) Tokuda, Y.; Yamashita, T.; Kamata, I.; Naijo, T.; Miyazawa, T.; Hayashi, S.; Hoshino, N.; Kato, T.; Okumura, H.; Kimoto, T.; et al. Structural analysis of double-layer Shockley stacking faults formed in heavily-nitrogen-doped 4H-SiC during annealing. *J. Appl. Phys.* **2017**, *122*, 045707.
(11) Harada, S.; Alexander; Seki, K.; Yamamoto, Y.; Zhu, C.; Yamamoto, Y.; Arai, S.; Yamasaki, J.; Tanaka, N.; Ujihara, T. Polytype Transformation by Replication of Stacking Faults Formed by Two-Dimensional Nucleation on Spiral Steps during SiC Solution Growth. *Cryst. Growth Des.* **2012**, *12*, 3209−3214.
(12) Ujihara, T.; Kozawa, S.; Seki, K.; Alexander; Yamamoto, Y.; Harada, S. Conversion Mechanism of Threading Screw Dislocation during SiC Solution Growth. *Mater. Sci. Forum* **2012**, *717*−*720*, 351−354.
(13) Ota, C.; Nishio, J.; Okada, A.; Iijima, R. Origin and Generation Process of a Triangular Single Shockley Stacking Fault Expanding from the Surface Side in 4H-SiC PIN Diodes. *J. Electron. Mater.* **2021**, *50*, 6504−6511.
(14) Hayashi, S.; Yamashita, T.; Senzaki, J.; Kato, T.; Yonezawa, Y.; Kojima, K.; Okumura, H. Relationship between depth of basal-plane dislocations and expanded stacking faults by application of forward current to 4H-SiC p-i-n diodes. *Appl. Phys. Express* **2019**, *12*, 051007.
(15) Iijima, A.; Kamata, I.; Tsuchida, H.; Suda, J.; Kimoto, T. Correlation between shapes of Shockley stacking faults and structures of basal plane dislocations in 4H-SiC epilayers. *Philos. Mag.* **2017**, *97*, 2736−2752.
(16) Maximenko, S. I.; Freitas, J. A.; Picard, Y. N.; Klein, P. B.; Myers-Ward, R. L.; Lew, K. K.; Muzykov, P. G.; Gaskill, D. K.; Eddy, C. R.; Sudarshan, T. S. CL/EBIC-SEM Techniques for Evaluation of Impact of Crystallographic Defects on Carrier Lifetime in 4H-SiC Epitaxial Layers. *Mater. Sci. Forum* **2010**, *645*−*648*, 211−214.
(17) Konishi, K.; Yamamoto, S.; Nakata, S.; Toyoda, Y.; Yamakawa, S. Driving Force of Stacking Fault Expansion in 4H-SiC PN Diode by in situ Electroluminescence Imaging. *Mater. Sci. Forum* **2014**, *778*−*780*, 342−345.
(18) Kamata, I.; Zhang, X.; Tsuchida, H. Photoluminescence Imaging and Wavelength Analysis of Basal Plane Frank-Type Defects in 4H-SiC Epilayers. *Mater. Sci. Forum* **2012**, *725*, 15−18.
(19) Zhang, X.; Ha, S. Y.; Benamara, M.; Skowronski, M.; Sumakeris, J. J.; Ryu, S. H.; Paisley, M. J.; O'Loughlin, M. J. Structure of Carrot Defects in 4H-SiC Epilayers. *Mater. Sci. Forum* **2006**, *527*−*529*, 327−332.
(20) Dorp, D. H. v.; Weyher, J. L.; Kelly, J. J. Anodic etching of SiC in alkaline solutions. *J. Micromech. Microeng.* **2007**, *17*, S50−S55.
(21) Geng, W.; Yang, G.; Zhang, X.; Zhang, X.; Wang, Y.; Song, L.; Chen, P.; Zhang, Y.; Pi, X.; Yang, D.; et al. Identification of subsurface damage of 4H-SiC wafers by combining photo-chemical etching and molten-alkali etching. *J. Semicond.* **2022**, *43*, 102801.
(22) Weyher, J. L.; Lazar, S.; Borysiuk, J.; Pernot, J. Defect-selective etching of SiC. *Phys. Status Solidi A* **2005**, *202*, 578−583.
(23) Nishio, J.; Ota, C.; Iijima, R. Structural study of single Shockley stacking faults terminated near substrate/epilayer interface in 4H-SiC. *Jpn. J. Appl. Phys.* **2022**, *61*, SC1005.
(24) Li, L. B.; Chen, Z. M.; Xie, L. F.; Yang, C. Lattice-matching of Si grown on 6H-SiC (000−1) C-face. *J. Cryst. Growth* **2014**, *385*, 111−114.
(25) Hähnel, A.; Pippel, E.; Woltersdorf, J. Control of Ni/SiC reactions by germanium, studied on the atomic scale. *Scripta Mater.* **2009**, *60*, 858−861.
(26) Kawahara, C.; Suda, J.; Kimoto, T. Identification of dislocations in 4H-SiC epitaxial layers and substrates using photoluminescence imaging. *Jpn. J. Appl. Phys.* **2014**, *53*, 020304.
(27) Kim, J.-H.; Cho, D.-H.; Lee, W.; Moon, B.-M.; Bahng, W.; Kim, S.-C.; Kim, N.-K.; Koo, S.-M. Structural and optical properties of epitaxial ZnO thin films on 4H-SiC (0001) substrates prepared by pulsed laser deposition. *J. Alloys Compd.* **2010**, *489*, 179−182.
(28) Luo, H.; Li, J.; Yang, G.; Zhu, R.; Zhang, Y.; Wang, R.; Yang, D.; Pi, X. Electronic and Optical Properties of Threading Dislocations in *n*-Type 4H-SiC. *ACS Appl. Energy Mater.* **2022**, *4*, 1678−1683.
(29) Lu, W.; Tarekegne, A. T.; Ou, Y.; Kamiyama, S.; Ou, H. Temperature-dependent photoluminescence properties of porous fluorescent SiC. *Sci. Rep.* **2019**, *9*, 16333.
(30) Liu, J.; Liu, Z.; Ren, P.; Xu, P.; Chen, X.; Xu, X. Fabrication and Luminescent Properties of 6H-SiC/3C-SiC/6H-SiC Quantum Well Structure. *Acta Phys.-Chim. Sin.* **2008**, *24*, 571−575.
(31) Sbruev, I. S.; Sbruev, S. B. Quantum wells on 3C-SiC/NH-SiC heterojunctions. Calculation of spontaneous polarization and electric field strength in experiments. *Semiconductors* **2010**, *44*, 1313−1320.
(32) Bauer, M.; Gigler, A. M.; Huber, A. J.; Hillenbrand, R.; Stark, R. W. Temperature-depending Raman line-shift of silicon carbide. *J. Raman Spectrosc.* **2009**, *40*, 1867−1874.
(33) Harima, H.; Nakashima, S.; Uemura, T. Raman scattering from anisotropic LO-phonon-plasmon-coupled mode in *n*-type 4H- and 6H-SiC. *J. Appl. Phys.* **1995**, *78*, 1996−2005.
(34) Yang, Y.; Guo, J.; Raghothamachar, B.; Chan, X.; Kim, T.; Dudley, M. Characterization of Strain Due to Nitrogen Doping Concentration Variations in Heavy Doped 4H-SiC. *J. Electron. Mater.* **2018**, *47*, 938−943.
(35) Hashiguchi, T.; Ota, T.; Asano, S.; Ohtani, N. Enhanced nitrogen incorporation in the < 11−20> directions on the (000−1) facet of 4H-SiC crystals. *Jpn. J. Appl. Phys.* **2022**, *61*, 095501.
(36) Izawa, T.; Okano, H.; Morita, S.; Ohtani, N. Influence of the facet trace region in 4H-SiC substrate on the glide and propagation behaviors of basal plane dislocations in 4H-SiC homoepitaxial layers. *J. Appl. Phys.* **2021**, *130*, 095702.
(37) Gao, B.; Kakimoto, K. Three-dimensional modeling of basal plane dislocations in 4H-SiC single crystals grown by the physical vapor transport method. *Cryst. Growth Des.* **2014**, *14*, 1272−1278.
(38) Nakano, T.; Shinagawa, N.; Yabu, M.; Ohtani, N. Formation and multiplication of basal plane dislocations during physical vapor transport growth of 4H-SiC crystals. *J. Cryst. Growth* **2019**, *516*, 51−56.
(39) Sonoda, M.; Nakano, T.; Shioura, K.; Shinagawa, N.; Ohtani, N. Structural characterization of the growth front of physical vapor transport grown 4H-SiC crystals using X-ray topography. *J. Cryst. Growth* **2018**, *499*, 24−29.
(40) Zhang, J.; Liang, T.; Lu, Y.; Xu, B.; Deng, T.; Zhang, Y.; Zeng, Z.; Pi, X.; Yang, D.; Wang, R. Effect of hexagonality on the pressure-dependent lattice dynamics of 4H-SiC. *New J. Phys.* **2022**, *24*, 113015.

https://doi.org/10.1021/acs.jpcc.3c01502
J. Phys. Chem. C 2023, 127, 13767−13772